Weighing an Optically Trapped Microsphere in Thermal Equilibrium With Air

L.E. Hillberry⬤,[*] Y. Xu⬤, S. Miki-Silva⬤, G.H. Alvarez⬤, J.E. Orenstein, L.C. Ha, D.S. Ether⬤, and
M.G. Raizen

*Center for Nonlinear Dynamics and Department of Physics, The University of Texas at Austin, Austin,
Texas 78712-1081, USA*

We report a weighing metrology experiment of a single silica microsphere optically trapped and immersed in air. Based on fluctuations about thermal equilibrium, three different mass measurements are investigated, each arising from one of two principle methods. The first method is based on spectral analysis and enables simultaneous extraction of various system parameters. Additionally, the spectral method yields a mass measurement with systematic relative uncertainty of 3.0% in 3 s and statistical relative uncertainty of 0.9% across several trapping laser powers. Parameter values learned from the spectral method serve as input, or a calibration step, for the second method based on the equipartition theorem. The equipartition method gives two additional mass measurements with systematic and statistical relative uncertainties slightly larger than those obtained in the spectral method, but over a time interval 10 times shorter. Our mass estimates, which are obtained in a scenario of strong environmental coupling, have uncertainties comparable to ones obtained in force-driven metrology experiments with nanospheres in vacuum. Moreover, knowing the microsphere's mass accurately and precisely will enable air-based sensing applications.

I. INTRODUCTION

Optical trapping of nano- and microscale objects [1–3] has become a paradigmatic tool in diverse fields, from micromanipulation of biological samples [4–15] to center-of-mass cooling experiments [16–18] aiming to observe macroscopic quantum effects [19–21], to metrology experiments [22–24] with optomechanical sensing applications [25–29]. In such experiments, a tightly focused laser beam, named the optical tweezer [30–32], is used to polarize a dielectric particle and harmonically confine it to the beam's intensity maximum.

It is often desirable to monitor the trapped particle's position as a function of time, so a position-sensitive detector must be calibrated. Calibrating the detector usually requires knowledge of the trapped particle's mass [22]. However, SiO_2 nano- and microspheres, often the object of study in levitated optomechanics experiments, do not have a readily known mass. The Stöber process used to manufacture these particles [33] yields very spherical results with a low dispersion of radius (approximately 3%), but a mass density that can vary in excess of 20% [33,34]. Calculated with these values, the uncertainty in mass is about 22%. For this reason, recent work has focused on mass metrology of nano- and microspheres optically trapped

in vacuum using methods of electrostatic levitation [34], oscillation [23], and trapping potential nonlinearities [24], and, most recently, a drop-recapture method performed in air [35]. The mass uncertainty achieved in each of these experiments is at the level of one to a few percent. Each has unique advantages like no assumptions on particle geometry, and distinct challenges, e.g., control of the particle's charge, accurate modeling of local potentials (gravitational, electric, or optical), or vacuum capabilities including feedback cooling.

Here, we report on a mass metrology experiment with uncertainty similar to previous work, but performed on a 1.5 μm radius SiO_2 microsphere optically trapped in air [36] at room temperature and pressure. Our experiment employs a dual-beam optical trap [1,37], sketched in Fig. 1(a) and elaborated upon in Ref. [38]. Our system remains in thermal equilibrium at all times making for a simple protocol. Moreover, we explore two distinct methodologies leveraging our detector's high spatiotemporal resolution. In the first *spectral method*, we fit an average voltage signal power spectral density (PSD) to simultaneously extract parameters that make no assumptions on the physical conditions of the experiment. We then fix conditions known with high accuracy—the air temperature, air viscosity, and particle radius—to compute the harmonic trap strength k, microsphere mass density ρ, and detector calibration factor β, as well as the uncertainties and correlations of these parameters. The microsphere
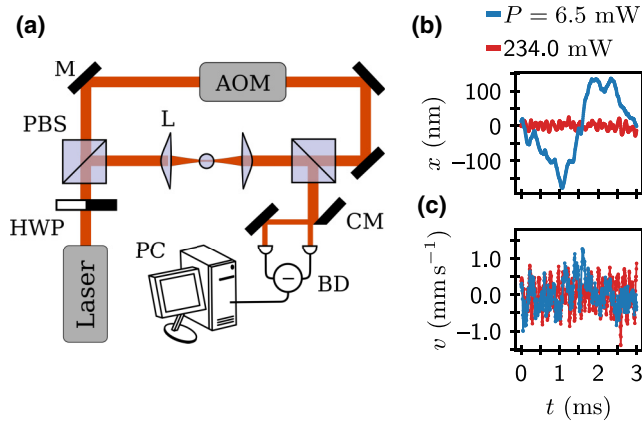
————
[*]lhillber@utexas.edu

FIG. 1. (a) Schematic of the dual beam optical trap and the detection system, comprising dielectric mirrors (M), half-wave plate (HWP), polarizing beam splitter (PBS), acoustic optical modulator (AOM), aspheric lens (L), cut mirror (CM), balanced photodetector (BD), personal computer (PC). (b) An example position trace at high and low trapping powers. (c) An example velocity trace that is computed with an eighth-order-accuracy numeric finite difference [38] of the data in (b).

mass is similarly calculated by combining fitting and fixed parameters.

In the second *equipartition method*, we compute the voltage signal and voltage-derivative signal variances from which we deduce the particle mass in two additional ways. Doing so requires a detector with sufficient resolution to observe the particle's instantaneous velocity, pioneered in Refs. [16,39]. The equipartition methods additionally require knowledge of either the harmonic trap strength k or calibration factor β that must be determined via the spectral method first. The spectral method demands a high volume of data to sufficiently smooth the experimental PSD, and is in that sense slow. The equipartition methods, once an initial spectral calibration is performed, require 10 times less data to achieve similar uncertainty in subsequent mass measurements.

Making precise and fast mass measurements in a system strongly coupled to the environment might have applications in scenarios where either the mass changes with time but the temperature is fixed, for instance in heterogeneous nucleation [40,41], or the mass is fixed but the temperature changes, like in Rayleigh-Bénard convection [42,43].

This paper is organized as follows. First, we review the relevant physics and outline our PSD parameter estimation method in Sec. II. In Sec. III we show how the PSD parameters, along with the equipartition theorem, allow us to weigh the microsphere in three different ways. There, we also present the results that we further discussion in Sec. IV. Finally, we conclude with this work's significance in Sec. V.

II. POWER SPECTRAL DENSITY PARAMETER ESTIMATION

The dynamics of the trapped microsphere along the x axis may be modeled by the harmonically bound Langevin equation of motion

$$m\ddot{x} + \gamma\dot{x} + kx = F(t), \tag{1}$$

where $m = 4\pi\rho R^3/3$ is the mass of the microsphere with radius R and density ρ, $\gamma = 6\pi\eta R$ is the Stokes friction coefficient, η is the viscosity of air, and k is the trap strength. The stochastic thermal force $F(t) = g\xi(t)$ is assumed to have the form of zero-mean $\langle\xi(t)\rangle = 0$, delta-correlated $\langle\xi(t)\xi(t')\rangle = \delta(t - t')$ white noise with strength $g = \sqrt{2k_BT\gamma}$ (according to the fluctuation-dissipation theorem), and in which T is the air temperature, k_B is Boltzmann's constant, and $\langle\cdot\rangle$ denotes ensemble averages over realizations of ξ. Writing Eq. (1) in terms of the Fourier transforms $\tilde{x}(\omega)$ and $\tilde{F}(\omega)$ [44] lets one deduce the position PSD $S_x(\omega)$ such that $\langle\tilde{x}(\omega)\tilde{x}(\omega')\rangle = S_x(\omega)\delta(\omega - \omega')$ [45], where $\omega = 2\pi f$ is the angular frequency.

In our experiment, we record a unitless voltage signal $V(t) = V_-(t)/V_+(0)$, where $V_-(t)$ is proportional to the difference in optical power delivered to the two ports of the balanced photodetector at time t and $V_+(0)$ is proportional to the total detection power at time $t = 0$. Normalizing the signal in this way accounts for small variations in detected power upon changing the trapping laser power. Here $V(t)$ is proportional to the microsphere's position along the x axis: $x(t) = V(t)/\beta$, where β is the calibration factor that we report in units of μm^{-1}.

From such considerations, the theoretical (one-sided) PSD of our voltage signal is understood to be

$$S_V(\omega) = \beta^2 \frac{4k_BT\gamma}{(m\omega^2 - k)^2 + \gamma^2\omega^2}. \tag{2}$$

Multiple trials of experimental power spectra must be averaged together before we attempt to learn relevant physical parameters. We collect ten trials of the voltage signal, each 0.3 s long, at a sampling rate of 50 MHz. In postprocessing, the signal is low-pass filtered by averaging together nonoverlapping blocks of 256 samples for improved spatial resolution. The new effective sampling rate is 195 kHz. Using *Bartlett's method* [38,46] with four windows per trial—for a total of 40 averages of length $\mathcal{T} = 84$ ms—we estimate the experimental voltage PSD, denoted $\hat{S}_{V,k} = \hat{S}_V(f_k)$. The index k labels the discrete frequencies at which the experimental PSD is known. The frequency resolution is $f_{k+1} - f_k = \mathcal{T}^{-1}$.

Once a set of trials is collected, we fit the experimental data $\hat{S}_V$ to

$$S_V(f; \boldsymbol{\theta}) = \frac{1}{a + bf^2 + cf^4}, \tag{3}$$

in which we have defined the column vector of free parameters $\boldsymbol{\theta} = (a, b, c)^\top$. In particular, the fit is done using the maximum likelihood estimation method [47–49] that we briefly outline next.

First, note that each data point of an n-trial-averaged PSD is subject to gamma-distributed noise (the convolution of n exponential distributions) [48,50], written

$$\mathcal{P}(\hat{S}_{V,k}) = \frac{1}{S_{V,k}} \frac{n^n}{\Gamma(n)} \left(\frac{\hat{S}_{V,k}}{S_{V,k}} \right)^{n-1} \exp\left(-n \frac{\hat{S}_{V,k}}{S_{V,k}} \right), \quad (4)$$

where $\Gamma(n) = (n-1)!$ is the gamma function and $S_{V,k}$ is the mean value of the distribution. Then, the likelihood of measuring the entire data set data $\hat{S}_V$ given a model $S_{V,k} = S_V(f_k, \boldsymbol{\theta})$ is the joint distribution

$$\mathcal{P}(\hat{S}_V \mid \boldsymbol{\theta}) = \prod_k \mathcal{P}(\hat{S}_{V,k}). \quad (5)$$

Maximizing the likelihood (5) is equivalent to minimizing the negative log likelihood

$$\mathcal{L}(\boldsymbol{\theta}, \hat{S}_V) = n \sum_k \left(\log[S_V(f_k; \boldsymbol{\theta})] + \frac{\hat{S}_V(f_k)}{S_V(f_k; \boldsymbol{\theta})} \right) + C, \quad (6)$$

where $C = \sum_k [\log \Gamma(n) - n \log n - (n-1) \log \hat{S}_V(k)]$ is a constant with respect to the free parameters and thus inconsequential for the minimization, and $n = 40$ is the number of spectra averaged together in the experiment.

Good starting values for the minimization can be calculated analytically and implemented numerically, a convenient feature that is not possible if one attempts to fit directly to Eq. (2) [48]. Maximum likelihood fitting accounts for the gamma-distributed PSD data, unlike more common least-squares fitting algorithms that assume normally distributed noise and thus provide biased PSD parameter estimations [48]. In the end, the minimization gives the best-fit parameters $\hat{\boldsymbol{\theta}} = (\hat{a}, \hat{b}, \hat{c})^\top$ that maximize the likelihood of the data given the model $\mathcal{P}(\hat{S}_V \mid \boldsymbol{\theta}) = \exp[-\mathcal{L}(\boldsymbol{\theta}, \hat{S}_V)]$. In Fig. 2(a) we show experimental PSD and the best-fit curve for two different trapping laser powers and compare to the noise inherent to the detection system. To measure the parameter fitting uncertainty and correlation, and inspired by the *profile likelihood* method [47,49], we scan $\boldsymbol{\theta}$ in the vicinity of $\hat{\boldsymbol{\theta}}$ over a volume of parameter space to build up a three-variate probability distribution $\mathcal{P}$ [see Figs. 2(b) and 2(c)] that is fit to a three-variate Gaussian distribution

$$\mathcal{P}_G(\boldsymbol{\theta}; \hat{\boldsymbol{\theta}}, \boldsymbol{\Sigma}_\theta) = \exp\left[-\tfrac{1}{2}(\boldsymbol{\theta} - \hat{\boldsymbol{\theta}})^\top \boldsymbol{\Sigma}_\theta^{-1}(\boldsymbol{\theta} - \hat{\boldsymbol{\theta}}) \right]. \quad (7)$$

The absolute residuals $|\mathcal{P} - \mathcal{P}_G|$ are bound below the 1% level. The 95th percentile is bound below the 0.1% level [38]. The vector $\hat{\boldsymbol{\theta}}$ resulting from the fit is taken as the best-fit parameter set. The matrix $\boldsymbol{\Sigma}_\theta$ resulting from the fit provides the variance-covariance matrix of the fitted parameters:

$$\boldsymbol{\Sigma}_\theta = \begin{pmatrix} \sigma_a^2 & \sigma_{ab}^2 & \sigma_{ac}^2 \\ \sigma_{ab}^2 & \sigma_b^2 & \sigma_{bc}^2 \\ \sigma_{ac}^2 & \sigma_{bc}^2 & \sigma_c^2 \end{pmatrix}.$$

The uncertainty in parameter i is $\sigma_i = ([\boldsymbol{\Sigma}_\theta]_{i,i})^{1/2}$ and the correlation coefficient between parameters i and j is $r_{i,j} = [\boldsymbol{\Sigma}_\theta]_{i,j}/(\sigma_i \sigma_j)$ for $i, j = a, b, c$ (see Ref. [38] for a visualization).

The fitting parameters $\boldsymbol{\theta}$ may be used to deduce a more physical set of parameters: trap strength k, microsphere density ρ, and calibration constant β. Each of the physical parameters $\boldsymbol{\Theta} = (k, \rho, \beta)^\top$ are a function of the fitting parameters and constant parameters R, T, and η. That is, $\boldsymbol{\Theta} = \boldsymbol{\Theta}(\boldsymbol{\phi})$, where we have defined the vector of independent variables $\boldsymbol{\phi} = (\boldsymbol{\theta}, R, \eta, T)^\top$ (explicit formulae are given in the Appendix). We now turn to the uncertainty analysis of the constant parameters.

The microsphere radius is known to be $R = 1.51$ μm up to 3.0% uncertainty based on statistical analysis of approximately 200 microspheres imaged with a scanning electron microscope [51]. Similar image analysis suggests $\epsilon = a/b - 1$ to be 0.027, where $a/b \geq 1$ is the aspect ratio of the imaged microspheres. To first order in ϵ, we estimate corrections to the Stokes friction coefficient due to aspherical geometry [52] to be less than 1%. Similar estimations apply to the microsphere volume, so uncertainty in the radius dominates uncertainty in the geometry. The air temperature, measured with a thermocouple before each trial, is found to vary less than 0.05% over the entire experimental run. The viscosity of air, calculated as a function of temperature with Sutherland's model, is found to vary over a similarly small range [38,53]. Sutherland's model is known to interpolate experimental viscosity data near room temperature with an uncertainty below 0.09%, including effects of up to 10% humidity [54]. Since the experiment is performed at atmospheric pressure, the particle-environment interaction is outside the Knudsen regime [55]. As a result, no laser-induced heating of the microsphere is expected, and so thermal equilibrium is assumed.

In light of these observations, the variance-covariance matrix of fitting and constant parameters may be approximated in the block-diagonal form diag($\boldsymbol{\Sigma}_\theta, \sigma_R^2, 0, 0$), where the last two zeros reflect the small relative uncertainty in T and η compared to that in a, b, c, and R. The block-diagonal form assumes correlation exists only between the fitted parameters.
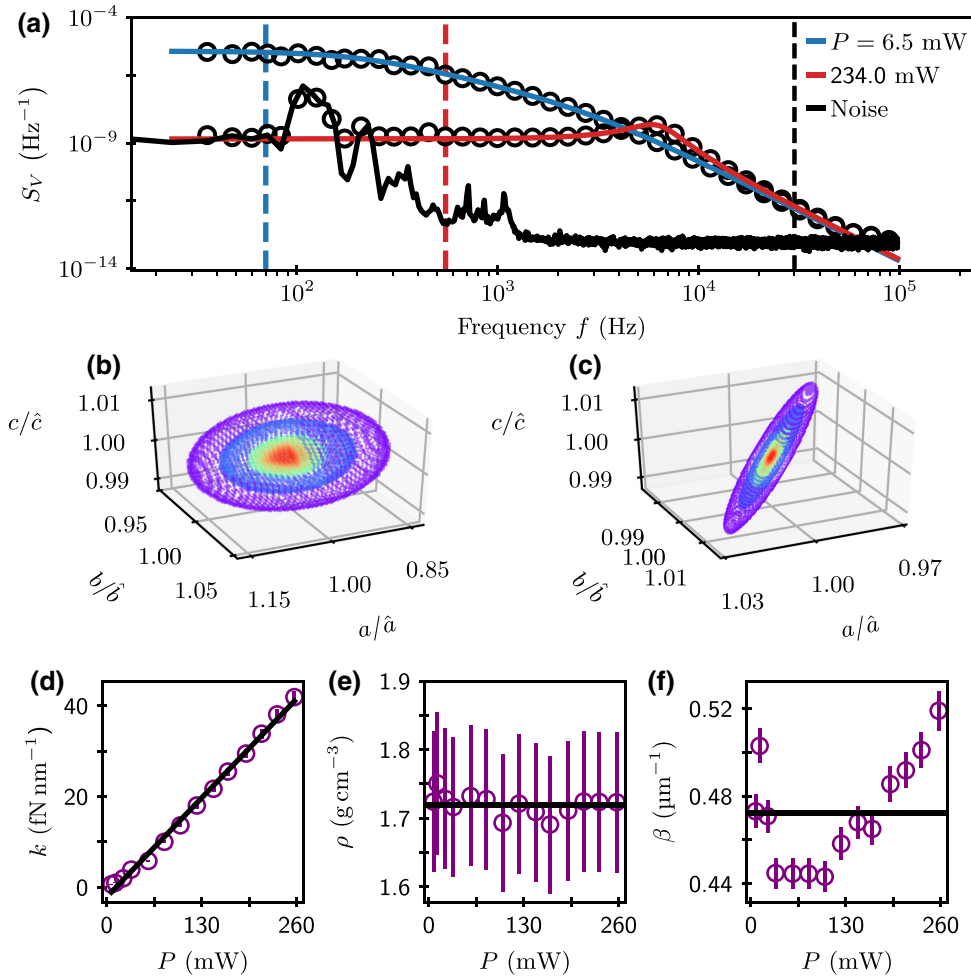
FIG. 2. (a) Voltage PSD for 6.5 (blue) and 234.0 mW (red) of trapping laser power. Experimental data is depicted with open circles and consists of 40 independent PSD averages and further bin averaged on a logarithmic horizontal scale for visualization purposes. The solid lines are the maximum likelihood best fit to Eq. (3). The vertical dashed lines mark the bounds on the data used in the fit. The lower bound is color coded with the fitting line and the upper bound (black dashed line) is shared. The noise spectrum (solid black) is collected under identical detection conditions as the other two curves but with no microsphere present. We see a technical noise floor at high frequencies and electronic-laser noise, including 60 Hz harmonics and $1/f$ noise, at low frequencies. The noise peak at around 120 Hz must be omitted when fitting the 234.0 mW spectrum, as indicated by the lower bound (red dashed line). (b) For 6.5 mW of laser power, we plot the isosurfaces of $\mathcal{P} = \exp(-\mathcal{L})$ [see Eq. (6)] as a function of fitting parameters $\boldsymbol{\theta}$. The isosurfaces are taken at Gaussian widths of 3 sigma (purple), 2 sigma (blue), and a core from the peak (red) to the 1-sigma width (green). (c) As in (b) but for 234.0 mW of trapping laser power. By fitting the likelihood data clouds shown in (b) and (c) to a three-variate Gaussian distribution, we extract the best-fit parameters $\hat{\boldsymbol{\theta}}$ and the variance-covariance matrix $\boldsymbol{\Sigma_\theta}$. (d) Trap strength k, (e) microsphere mass density ρ, and (f) calibration constant β, each extracted from PSD fits as a function of laser power P. In (d)–(f), error bars reflect systematic uncertainty calculated by error propagation, including correlation among fitted parameters.

We calculate the variance-covariance matrix of the physical parameters in terms of the fitting and constant parameters via the error propagation equation [56] $\boldsymbol{\Sigma_\Theta} = \boldsymbol{J_\Theta \Sigma_\phi J_\Theta^\top}$. The Jacobian matrix (evaluated at the optimal fitting parameters) is $(J_\Theta)_{i,j} = [\partial\Theta_i/\partial\phi_j]_{\boldsymbol{\theta}=\hat{\boldsymbol{\theta}}}$. We have verified that the parameters and uncertainties deduced by the procedure described here and conveniently visualized in Figs. 2(b)–2(c) agree quantitatively with the Monte Carlo method that generates and fits many artificial PSDs by sampling the appropriate gamma distribution. Our

technique yields directly the probability density, sidestepping the need for binning and fitting or kernel-density estimating the Monte Carlo results.

We now understand how to estimate k, ρ, and β, including uncertainty and correlation, from an experimental voltage PSD $\hat{S}_V$. The results are presented in Figs. 2(d)–2(f) for experiments on the same trapped microsphere and that scan the trapping laser power from 6.5 to 257.2 mW. We observe no unexpected dependence of the physical parameters on laser power except for the calibration constant

that exhibits a nonmonotonic curve, first decreasing then increasing with laser power [Fig. 2(d)]. Thus, we conclude that heating of the microsphere due to the laser is inconsequential because of the strong environmental coupling. This is not the case for experiments in vacuum [55]. The trend in β is reproducible when the experiment is repeated with different microspheres, suggesting the source is most likely slight beam deviations caused by the HWP-PBS pairs used to control the trapping and detected power.

III. MASS MEASUREMENT TECHNIQUE

Upon learning PSD fitting parameters, presented in Sec. II, it is straightforward to estimate the mass using the density and radius of the microsphere. However, the equipartition theorem, $k_B T = m\langle \dot{x}^2 \rangle = k\langle x^2 \rangle$, provides two additional possibilities. The three mass measurements written in terms of the augmented independent variables $\boldsymbol{\phi}' = (a, b, c, \langle \dot{V}^2 \rangle, \langle V^2 \rangle, R, \eta, T)^\top$ read

$$m_1(\boldsymbol{\phi}') = \frac{4}{3}\pi R^3 \rho, \tag{8}$$

$$m_2(\boldsymbol{\phi}') = \frac{k_B T}{\langle \dot{V}^2 \rangle}\beta^2, \tag{9}$$

$$m_3(\boldsymbol{\phi}') = \frac{\langle V^2 \rangle}{\langle \dot{V}^2 \rangle}k. \tag{10}$$

The benefit of m_2 and m_3 is that, once a PSD fit is used to calibrate the system, further data can be collected to estimate the variances $\langle \dot{V}^2 \rangle$ and $\langle V^2 \rangle$, which may be used to update the mass measurement in the case it changes with time. Of course, there is nothing to update if the mass is unchanging. Nonetheless, to make use of methods m_2 or m_3, we must make an adequate estimate of the required variances. In Figs. 3(a) and 3(b) we show the histograms of position and velocity (proportional to V and $\dot{V}$, respectively) for high and low trapping laser powers. The histograms consist of data from a single 0.3 s trial. Overlaid on each histogram are Gaussian fits with variance as the only free parameter. Uncertainty in the variance calculation is taken as the standard deviation of variances calculated across ten trials.

For an uncorrelated voltage trace of length τ, the uncertainty in the variance estimate scales as $\tau^{-1/2}$, which is a thermally limited trend. However, at short times ($\tau < m/\gamma$), the data is correlated due to the microsphere's dynamics and, at long times, slow drifts in the system tend to affect the signal's variance. One way to quantify those correlations and to determine the optimal time over which our measurements are thermally limited is performing an Allan-deviation stability analysis [22,28,57,58].
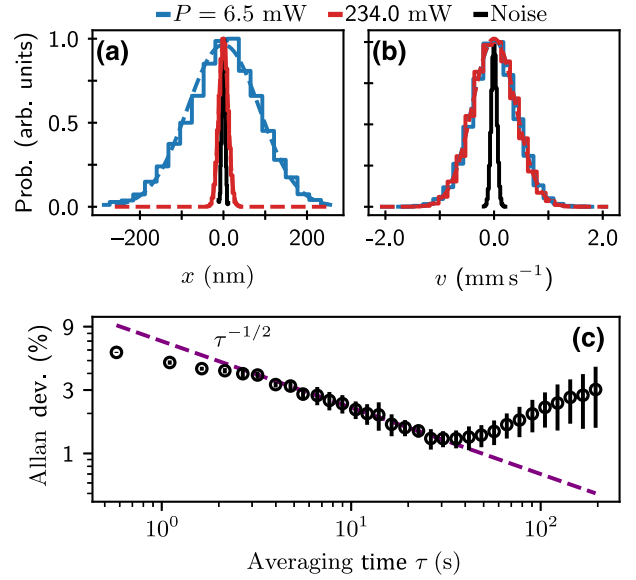

FIG. 3. (a) Position probability density (solid steps) of the microsphere's position over a single 0.3 s trial for 6.5 (blue) and 234.0 mW (red) of trapping laser power. Dashed lines correspond to a Gaussian fit with variance as the only free parameter. The black line is a histogram of the signal when no microsphere is present. (b) Velocity probability density. Colors are shared with (a). As expected by the equipartition theorem, the width of the position probability density gets narrower with increasing laser power while the width velocity probability density remains constant. All curves in (a),(b) are normalized by their maximum value. (c) The relative Allan deviation of variance calculated from a 14 min voltage signal decreases with increasing averaging time according to a $-1/2$ power law. The decay trend continues until a minimum of about 1% is reached in 30 s. Normalization is provided by the value of variance corresponding to the minimum Allan deviation. Error bars reflect the standard deviation of three trials.

In Fig. 3(c) we show the results of our Allan-deviation experiment performed with 22.8 mW of trapping laser power. Accordingly, our system is stable out to about 30 s, so using 0.3 s of data for estimating the variances allows for 100 independent mass measurements before the slow drifts demand recalibration of the apparatus. It is in this sense that methods m_2 and m_3 are faster than m_1.

In Fig. 4 we show the results of our three mass measurement procedures. We find $\bar{m}_1 = 24.8$ pg, $\bar{m}_2 = 25.1$ pg, and $\bar{m}_3 = 27.4$ pg, where the over bar denotes an average over the 14 experiments at different total trapping laser powers. Error bars reported are calculated [38] by considering covariance of the PSD fitting parameters, and uncertainties in both fixed parameters and variances. We consider such error bars systematic uncertainty, denoted $\sigma_{m_i}^{\text{sys}}$, $i = 1, 2, 3$. The statistical uncertainty (or fluctuation), denoted $\sigma_{m_i}^{\text{stat}}$, is calculated as the standard deviation across the 14 experiments at different laser powers. Measurement m_1, which is based entirely on the PSD analysis, has
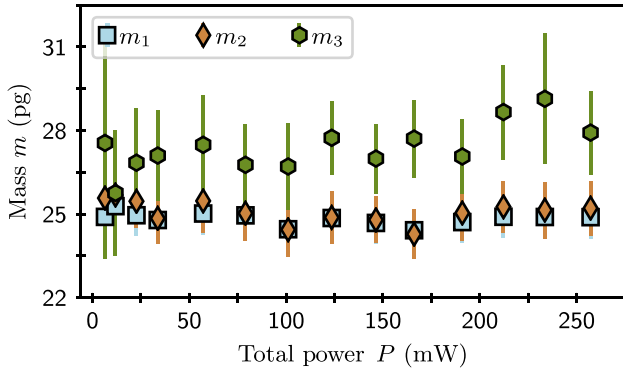
FIG. 4. Mass measurement comparison: blue squares, orange diamonds, and green hexagons respectively denote m_1, m_2, and m_3. Mass measurements as the total trapping power P is varied. Error bars denote the systematic uncertainties $\sigma_{m_i}^{\text{sys}}$, $i = 1, 2, 3$. Statistical uncertainties $\sigma_{m_i}^{\text{stat}}$ are calculated as standard deviations across the ensemble of mass estimates at different laser powers.

the smallest relative error bars ($\bar{\sigma}_{m_1}^{\text{sys}}/\bar{m}_1 = 3.0\%$) and the smallest relative statistical uncertainty ($\sigma_{m_1}^{\text{stat}}/\bar{m}_1 = 0.9\%$). Measurement m_2, which supplements the PSD analysis by estimating the voltage-derivative variance, agrees well with m_1, albeit with relative error bars at 4.1% and relative statistical fluctuations at 1.6%. The benefit of m_2 is that, once an initial PSD analysis is performed, parameters like mass (or temperature) can be subsequently updated 10 times faster than collecting data for additional PSD analysis. Measurement m_3 has the largest systematic and statistical relative uncertainties, 6.7% and 3.0%, respectively. Furthermore, method m_3 displays additional systematic error because it deviates from m_1 and m_2 by nearly 10%. We speculate on the source of this uncertainty in the next section.

For comparison, the mass according to the manufacturer values of density $\rho_{\text{Bangs}} = 2.0\,\text{g cm}^{-3}$ ($\sigma_{\rho_{\text{Bangs}}}/\rho_{\text{Bangs}} = 20\%$) and our radius measurement $R = 1.51\,\mu\text{m}$ ($\sigma_R/R = 2.9\%$) is $m_{\text{Bangs}} = 28.84$ pg with an uncertainty of 22% that agrees within the uncertainty tolerance of all our mass measurements, despite the discrepancy of the mean values.

IV. DISCUSSION

The systematic bias in m_3 of Fig. 4 is hypothesized to be dominated by the low-frequency electronic noise apparent in Fig. 2(a). By selecting an appropriate lower bound for the fit, the spectral method easily removes the influence of the noise resonances, the most severe of which appears at 120 Hz with a width of about 100 Hz. However, the time domain estimate of $\langle V^2 \rangle$ includes variance due to that noise. To estimate the effects of such noise, we can model the experimental PSD as the sum of the best-fit PSD and the experimental noise PSD containing the noise peak near 120 Hz, $S_V(f) = \bar{S}_V^{\text{best}}(f) + S_V^{\text{noise}}(f)$. Using Parseval's

theorem, $\langle q^2 \rangle = \int_0^\infty S_q(f)\, df$, we have

$$\langle V^2 \rangle \approx \langle V^2 \rangle_{\text{PSD}} + \int_{70\ \text{Hz}}^{170\ \text{Hz}} S_V^{\text{noise}}(f)\, df, \qquad (11)$$

where $\langle V^2 \rangle$ is the variance of the voltage signal observed in the time domain, $\langle V^2 \rangle_{\text{PSD}} = k_B T \beta^2 / k$ is the variance estimate provided by the PSD parameters. The excess variance $\Delta \langle V^2 \rangle \equiv |\langle V^2 \rangle - \langle V^2 \rangle_{\text{PSD}}|$ is about 10% of $\langle V^2 \rangle_{\text{PSD}}$, which agrees with the discrepancy between m_3 and the other measurements. The quantity $\Delta \langle V^2 \rangle$ can also be estimated by numerically integrating the observed noise spectrum. We find [38] that the integral of the noise PSD in the frequency band 70–170 Hz predicts the observed excess variance and hence also the bias in m_3.

The effects of low-frequency noise resonances are suppressed when estimating $\langle \dot{V}^2 \rangle$. The reason is because, in general, $S_{\dot{q}}(f) = (2\pi f)^2 S_q(f)$, so high-frequency components of a signal have a quadratically larger weighting factor in the variance compared to low-frequency noise. We find, by direct calculation on our data, that $\Delta \langle \dot{V}^2 \rangle \sim 2\%$, which agrees with the numeric integration of $S_{\dot{V}}^{\text{noise}}(f)$ over all frequencies above 80 kHz [38].

A recent experimental effort [23] measured the mass of 0.143 μm radius SiO$_2$ spheres optically trapped in vacuum to be 4.01 fg with 2.8% uncertainty with 40 s of position data. Their oscillating electric field method makes no assumption on particle shape or density, though a density of 2.2 g cm^{-3} agrees with their measurements. In Ref. [34], a 2.6 μm radius sphere is optically trapped and levitated with a static electric field as the trapping laser power is reduced, resulting in a mass measurement of 84 pg with 1.8% uncertainty with 42 min of data. The density is also measured to be 1.55 g cm^{-3} with 5.16% uncertainty. A third strategy used in Ref. [24] stabilizes oscillations of a 0.082 μm radius sphere in the nonlinear-trapping regime to deduce the detector calibration constant with 1.0% uncertainty and a mass of 3.63 fg with 2.2% uncertainty. Finally, very recent work [35] used a drop-recapture method and camera-based detection with time resolution that could not quite resolve the microsphere's instantaneous velocity. Fitting position autocorrelation functions, they measured their resin particle's radius to be 2.3 μm with 4.3% statistical uncertainty. In the drop-recapture experiments, 90 s worth of trials were used to deduce a mass of 55.8 pg with 1.4% statistical uncertainty and 13% systematic uncertainty. The authors combined the radius and mass measurements to deduce a density of 1.1 g cm^{-3} with 9.1% statistical uncertainty.

As a comparison, we present a summary of our physical parameter values and uncertainties in Table I. Based entirely on thermal equilibrium analysis, our two most accurate mass estimates have uncertainties of 3% to 4% as compared to the 1% to 2% uncertainty in

TABLE I. Table of values and uncertainties. Reported values are the average over the power scan experiment, except for k and $\langle V^2 \rangle$ for which we report the range since these quantities scale linearly with P. Also reported are the relative systematic uncertainties averaged over the power scan experiment and the statistical uncertainties that express the relative standard deviation over the power scan, where applicable.

Quantity	Value	Uncertainty (%)		Unit
		Systematic	Statistical	
R	1.51	2.9	…	μm
η	18.295	0.04	…	μPa s
T	295.50	0.05	…	K
$\langle \dot{V}^2 \rangle \times 10^3$	36.4	2.4	…	μs^{-1}
$\langle V^2 \rangle \times 10^3$	(0.03, 1.53)	8.9	…	Arb. units
k	(0.66, 49.1)	3.1	…	fN nm^{-1}
ρ	1.72	5.9	0.9	g cm^{-3}
β	0.47	1.6	5.0	μm^{-1}
m_1	24.8	3.0	0.9	pg
m_2	25.1	4.1	1.6	pg
m_3	27.4	6.7	3.0	pg

vacuum-dependent and 13% in the air-based, nonequilibrium methods. Furthermore, all of our measurements are made with significantly less position data. Interestingly, our density measurement has comparable accuracy to the recent body of work using SiO_2 particles, all of which sourced particles from the same manufacturer. The variability and apparent radius dependence of measured density values underscores the parameter's uncertainty inherent to the manufacturing process.

Most of the existing mass measurement methods are demonstrated in a high vacuum environment where the experimental goals often center around ground-state cooling or exceptionally sensitive force transduction. Additionally, the existing methods rely on forces external to the trap, often driving the system out of equilibrium and limiting their utility as environmental sensors. Our method has the advantages of speed in that between 10 and 100 times less data is required compared to other methods; environmental coupling, which unlocks future sensing applications; and simplicity in that no additional experimental setup is required beyond trapping and monitoring.

Disadvantages include the requirements of environmental coupling, enough spatiotemporal resolution to resolve the instantaneous velocity, and accurate knowledge of the particle radius. While an advantage for future applications, environmental coupling critically limits heating effects of the trapping laser and enables fast equilibration with the environment, so our method will face complications in vacuum-based experiments. Accurate heating-damping models and longer data traces could possibly overcome such concerns. Instantaneous velocity resolution enables our fastest measurement, m_2, but can be much more difficult in a liquid environment, though certainly possible [39]. Accurate knowledge of the trapped particle geometry is quantified statistically in our experiment, but less uniform samples could significantly alter the error analysis. In these cases, *in situ* measurements of the trapped particle with optical microscopy, light scattering, or autocorrelation function analysis could improve the error budget.

V. CONCLUSIONS

We explore spectral and equipartition methods by which to measure an optically trapped microsphere's mass while in thermal equilibrium with air. With the former, we accurately extract physical parameters of trap strength k, microsphere density ρ, and detector calibration constant β with 3 s of data. The initial spectral calibration step also yields the mass m_1 with 3.0% uncertainty. The subsequent equipartition method m_2 achieves an uncertainty of 4.1% in 0.3 s.

The work presented here demonstrates the sensitivity of optical tweezers in a scenario of strong environmental coupling, suggesting applications in air-based sensing. For example, single-site ice nucleation could be monitored in real time as a change in mass of the trapped particle. Alternatively, in a system of constant mass, one could first measure the mass using the spectral method and then use the equipartition method to measure changes in temperature within the trapping medium, which could be driven out of equilibrium with a temperature gradient to probe temperature-gradient-induced turbulence at small scales of space and time.

The equipartition theorem may be challenged by nonequilibrium dynamics. However, in the hydrodynamic regime where thermodynamic state variables are relevant in the sense of quasiequilibrium, we believe our method will be quite applicable. The small sensor size means that the dynamics are fast to respond to changes in the environment (on the scale of $m/\gamma \sim 45\ \mu$s in this work). Even in the complete absence of thermal equilibrium, where the notion of temperature is no longer defined, our position and velocity data may be used to compute more general velocity structure functions when the simple variance appearing in the equipartition theorem is insufficient [59,60]. We consider such nonequilibrium studies a fruitful direction for future optical tweezer experiments.

APPENDIX: PARAMETER CONVERSIONS

The physical parameters, denoted by the column vector $\mathbf{\Theta} = (k, \rho, \beta)^\top$, are functions of the independent variables $\mathbf{\phi} = (a, b, c, R, \eta, T)^\top$. First we define

$$d_1 \equiv b + \sqrt{ac}, \tag{A1}$$

$$d_2 \equiv b + 2\sqrt{ac}. \tag{A2}$$

Then, for $\mathbf{\Theta}(\mathbf{\phi})$, we have

$$k(\mathbf{\phi}) = 12\pi^2 \eta R \sqrt{\frac{a}{d_2}}, \tag{A3}$$

$$\rho(\mathbf{\phi}) = \frac{9\eta}{4\pi R^2} \sqrt{\frac{c}{d_2}}, \tag{A4}$$

$$\beta^2(\mathbf{\phi}) = \frac{6\pi^3 \eta R}{k_B T d_2}. \tag{A5}$$

The mass measurements $\mathbf{m} = (m_1, m_2, m_3)^\top$ are a function of the augmented independent variables, $\mathbf{\phi}' =$ $(a, b, c, \langle \dot{V}^2 \rangle, \langle V^2 \rangle, R, \eta)$ (noting that $\partial \mathbf{m} / \partial T = 0$). For explicit formulae, we have

$$m_1(\mathbf{\phi}') = 3\eta R \sqrt{\frac{c}{d_2}}, \tag{A6}$$

$$m_2(\mathbf{\phi}') = \frac{6\pi^3 \eta R}{d_2} \frac{1}{\langle \dot{V}^2 \rangle}, \tag{A7}$$

$$m_3(\mathbf{\phi}') = 12\pi^2 \eta R \sqrt{\frac{a}{d_2}} \frac{\langle V^2 \rangle}{\langle \dot{V}^2 \rangle}. \tag{A8}$$

We next define

$$u_1 \equiv \frac{3}{16\pi^3 R^3}, \qquad u_2 \equiv \frac{1}{2\sqrt{6\pi \eta R k_B T}}, \tag{A9}$$

$$v_1 \equiv \frac{1}{4\pi^2}, \qquad v_2 \equiv \frac{\pi}{\langle \dot{V}^2 \rangle}, \qquad v_3 \equiv \frac{\langle V^2 \rangle}{\langle \dot{V}^2 \rangle}, \tag{A10}$$

to write the Jacobians

$$\frac{\partial \mathbf{\Theta}}{\partial \mathbf{\phi}} = \frac{6\pi^2 \eta R}{\sqrt{a d_2^3}} \begin{pmatrix} d_1 & -a & -\sqrt{a^3/c} & 2ad_2/R & 2ad_2/\eta & 0 \\ -u_1 c & -u_1 \sqrt{ac} & u_1 d_1 \sqrt{a/c} & -4u_1 d_2 \sqrt{ac}/R & 2u_1 d_2 \sqrt{ac}/\eta & 0 \\ -u_2 \sqrt{c} & -u_2 \sqrt{a} & -u_2 a/\sqrt{c} & u_2 d_2 \sqrt{a}/R & u_2 d_2 \sqrt{a}/\eta & -u_2 d_2 \sqrt{a}/T \end{pmatrix}, \tag{A11}$$

$$\frac{\partial \mathbf{m}}{\partial \mathbf{\phi}'} = \frac{6\pi^2 \eta R}{\sqrt{a d_2^3}} \begin{pmatrix} -v_1 c & -v_1 \sqrt{ac} & v_1 d_1 \sqrt{a/c} & 0 & 0 & 2v_1 d_2 \sqrt{ac}/R & 2v_1 d_2 \sqrt{ac}/\eta \\ -v_2 \sqrt{c/d_2} & -v_2 \sqrt{a/d_2} & -v_2 a/\sqrt{cd_2} & -v_2 \sqrt{ad_2}/\langle \dot{V}^2 \rangle & 0 & v_2 \sqrt{ad_2}/R & v_2 \sqrt{ad_2}/\eta \\ v_3 d_1 & -v_3 a & -v_3 \sqrt{a^3/c} & -2v_3 ad_2/\langle \dot{V}^2 \rangle & 2v_3 ad_2/\langle V^2 \rangle & 2v_3 ad_2/R & 2v_3 ad_2/\eta \end{pmatrix}. \tag{A12}$$

[1] A. Ashkin, Acceleration and Trapping of Particles by Radiation Pressure, Phys. Rev. Lett. **24**, 156 (1970).

[2] A. Ashkin, History of optical trapping and manipulation of small-neutral particle, atoms, and molecules, IEEE J. Sel. Top. Quant. Electr. **6**, 841 (2000).

[3] A. Ashkin, *Optical Trapping and Manipulation of Neutral Particles Using Lasers: A Reprint Volume With Commentaries* (World Sci., Singapore, 2006).

[4] A. Ashkin and J. M. Dziedzic, Optical trapping and manipulation of viruses and bacteria, Science **235**, 1517 (1987).

[5] A. Ashkin, J. M. Dziedzic, and T. Yamane, Optical trapping and manipulation of single cells using infrared laser beams, Nature **330**, 769 (1987).

[6] K. C. Neuman and A. Nagy, Single-molecule force spectroscopy: Optical tweezers, magnetic tweezers and atomic force microscopy, Nat. Methods **5**, 491 (2008).

[7] B. Pontes, N. B. Viana, L. Campanati, M. Farina, V. M. Neto, and H. M. Nussenzveig, Structure and elastic properties of tunneling nanotubes, Eur. Biophys. J. **37**, 121 (2008).

[8] S. Frases, B. Pontes, L. Nimrichter, M. L. Rodrigues, N. B. Viana, and A. Casadevall, The elastic properties of the *Cryptococcus neoformans* capsule, Biophys. J. **97**, 937 (2009).

[9] B. Pontes, N. B. Viana, L. T. Salgado, M. Farina, V. M. Neto, and H. M. Nussenzveig, Cell cytoskeleton and tether extraction, Biophys. J. **101**, 43 (2011).

[10] E. Moeendarbary and A. R. Harris, Cell mechanics: Principles, practices, and prospects, WIREs Syst. Biol. Med. **6**, 371 (2014).

[11] M. P. Nicholas, L. Rao, and A. Gennerich, An improved optical tweezers assay for measuring the force generation of single kinesin molecules, Methods Mol. Biol. **1136**, 171 (2014).

[12] Y. A. Ayala, B. Pontes, D. S. Ether, L. B. Pires, G. R. Araujo, S. Frases, L. F. R. Ao, M. Farina, V. Moura-Neto, N. B. Viana, and H. M. Nussenzveig, Rheological properties of cells measured by optical tweezers, BMC Biophys. **9**, 5 (2016).

[13] H. M. Nussenzveig, Cell membrane biophysics with optical tweezers, Eur. Biophys. J. **47**, 499 (2018).

[14] H. M. Nussenzveig, Are cell membrane nanotubes the ancestors of the nervous system?, Eur. Biophys. J. **48**, 593 (2019).

[15] C. Bustamante, Y. R. Chemla, and J. R. Moffitt, High-resolution dual-trap optical tweezers with differential detection: Alignment of instrument components, Cold Spring Harb. Protoc. **161**, 260 (2009).

[16] T. Li, S. Kheifets, D. Medellin, and M. G. Raizen, Measurement of the instantaneous velocity of a brownian particle, Science **328**, 1673 (2010).

[17] J. Gieseler, B. Deutsch, R. Quidant, and L. Novotny, Sub-kelvin Parametric Feedback Cooling of a Laser-Trapped Nanoparticle, Phys. Rev. Lett. **109**, 103603 (2012).

[18] J. Gieseler, J. R. Gomez-Solano, A. Magazzù, I. P. Castillo, L. P. García, M. Gironella-Torrent, X. Viader-Godoy, F. Ritort, G. Pesce, A. V. Arzola, K. Volke-Sepulveda, and G. Volpe, Optical tweezers: A comprehensive tutorial from calibration to applications, arXiv:2004.05246 [physics.optics] (2020).

[19] R. Kaltenbaek et al., Macroscopic quantum resonators (maqro): 2015 update, EPJ Quantum Technol. **3**, 5 (2016).

[20] F. Tebbenjohanns, M. Frimmer, V. Jain, D. Windey, and L. Novotny, Motional Sideband Asymmetry of a Nanoparticle Optically Levitated in Free Space, Phys. Rev. Lett. **124**, 013603 (2020).

[21] U. Delić, M. Reisenbauer, K. Dare, D. Grass, V. Vuletić, N. Kiesel, and M. Aspelmeyer, Cooling of a levitated nanoparticle to the motional quantum ground state, Science **367**, 892 (2020).

[22] E. Hebestreit, M. Frimmer, R. Reimann, C. Dellago, F. Ricci, and L. Novotny, Calibration and energy measurement of optically levitated nanoparticle sensors, Rev. Sci. Instrum. **89**, 033111 (2018).

[23] F. Ricci, M. T. Cuairan, G. P. Conangla, A. W. Schell, and R. Quidant, Accurate mass measurement of a levitated nanomechanical resonator for precision force-sensing, Nano Lett. **19**, 6711 (2019).

[24] Y. Zheng, L.-M. Zhou, Y. Dong, C.-W. Qiu, X.-D. Chen, G.-C. Guo, and F.-W. Sun, Robust Optical-Levitation-Based Metrology of Nanoparticle's Position and Mass, Phys. Rev. Lett. **124**, 223603 (2020).

[25] G. Ranjit, D. P. Atherton, J. H. Stutz, M. Cunningham, and A. A. Geraci, Attonewton force detection using

microspheres in a dual-beam optical trap in high vacuum, Phys. Rev. A **91**, 051805(R) (2015).

[26] G. Ranjit, M. Cunningham, K. Casey, and A. A. Geraci, Zeptonewton force sensing with nanospheres in an optical lattice, Phys. Rev. A **93**, 053801 (2016).

[27] F. Monteiro, S. Ghosh, A. G. Fine, and D. C. Moore, Optical levitation of 10-ng spheres with nano-g acceleration sensitivity, Phys. Rev. A **96**, 063841 (2017).

[28] G. Schnoering, Y. Rosales-Cabara, H. Wendehenne, A. Canaguier-Durand, and C. Genet, Thermally Limited Force Microscopy on Optically Trapped Single Metallic Nanoparticles, Phys. Rev. Appl. **11**, 034023 (2019).

[29] J. Millen, T. S. Monteiro, R. Pettit, and A. N. Vamivakas, Optomechanics with levitated particles, Rep. Prog. Phys. **83**, 026401 (2020).

[30] A. Ashkin, J. M. Dziedzic, J. E. Bjorkholm, and S. Chu, Observation of a single-beam gradient force optical trap for dielectric particles, Opt. Lett. **11**, 288 (1986).

[31] A. Ashkin, How it all began, Nat. Photonics **5**, 316 (2011).

[32] A. Gennerich, ed., Optical Tweezers Methods and Protocols, Methods in Molecular Biology (Springer Science + Business Media, New York, 2017).

[33] W. Stöber, A. Fink, and E. Bohn, Controlled growth of monodisperse silica spheres in the micron size range, J. Colloid Interface Sci. **26**, 62 (1968).

[34] C. P. Blakemore, A. D. Rider, S. Roy, A. Fieguth, A. Kawasaki, N. Priel, and G. Gratta, Precision Mass and Density Measurement of Individual Optically Levitated Microspheres, Phys. Rev. Appl. **12**, 024037 (2019).

[35] G. Carlse, K. B. Borsos, H. C. Beica, T. Vacheresse, A. Pouliot, J. Perez-Garcia, A. Vorozcovs, B. Barron, S. Jackson, L. Marmet, and A. Kumarakrishnan, Technique for Rapid Mass Determination of Airborne Microparticles Based on Release and Recapture from an Optical Dipole Force Trap, Phys. Rev. Appl. **14**, 024017 (2020).

[36] Z. Gong, Y.-L. Pan, G. Videen, and C. Wang, Optical trapping and manipulation of single particles in air: Principles, technical details, and applications, J. Quant. Spectrosc. Radiat. Transform. **214**, 94 (2018).

[37] A. van der Horst, P. D. J. van Oostrum, A. Moroz, A. van Blaaderen, and M. Dogterom, High trapping forces for high-refractive index particles trapped in dynamic arrays of counterpropagating optical tweezers, Appl. Opt. **47**, 3196 (2008).

[38] See Supplemental Material at http://link.aps.org/supplemental/10.1103/PhysRevApplied.14.044027 for further details on the experimental setup, data processing, and uncertainty analysis.

[39] S. Kheifets, A. Simha, K. Melin, T. Li, and M. G. Raizen, Observation of brownian motion in liquids at short times: Instantaneous velocity and memory loss, Science **343**, 1493 (2014).

[40] S. Ishizaka, T. Wada, and N. Kitamura, In situ observations of freezing processes of single micrometer-sized aqueous ammonium sulfate droplets in air, Chem. Phys. Lett. **506**, 117 (2011).

[41] U. K. Krieger, C. Marcollia, and J. P. Reid, Exploring the complexity of aerosol particle properties and processes using single particle techniques, Chem. Soc. Rev. **41**, 6631 (2012).

[42] F. Chillà and J. Schumacher, New perspectives in turbulent rayleigh-bénard convection, Eur. Phys. J. E Soft Matter **35,** 58 (2012).

[43] K. P. Iyer, J. D. Scheel, J. Schumacher, and K. R. Sreenivasan, Classical 1/3 scaling of convection holds up to ra = 1015, Proc. Natl. Acad. Sci. **117,** 7594 (2020).

[44] The Fourier integrals are defined as $x(t) = (1/2\pi) \int_{-\infty}^{\infty} \tilde{x}(\omega) e^{-\imath\omega t} d\omega$ and $\tilde{x}(\omega) = \int_{-\infty}^{\infty} x(t')e^{\imath \omega t'}dt'$.

[45] L. Mandel and E. Wolf, *Optical Coherence and Quantum Optics* (Cambridge University Press, New York, 1995).

[46] A. V. Oppenheim, R. W. Schafer, and J. R. Buck, *Discrete-Time Signal Processing* (Prentice Hall, Upper Saddle River, NJ, 2001), p. 836.

[47] S. R. Cole, H. Chu, and S. Greenland, Maximum likelihood, profile likelihood, and penalized likelihood: A primer, Am. J. Epidemiol. **179,** 252 (2014).

[48] S. F. Norrelykke and H. Flyvbjerg, Power spectrum analysis with least-squares fitting: Amplitude bias and its elimination, with application to optical tweezers and atomic force microscope cantilevers, Rev. Sci. Instrum. **81,** 075103 (2010).

[49] C. Dawson and J. Bateman, Spectral analysis and parameter estimation in levitated optomechanics, JOSA B **36,** 1565 (2019).

[50] K. Berg-Sorensen and H. Flyvbjerg, Power spectrum analysis for optical tweezers, Rev. Sci. Instrum. **75,** 594 (2004).

[51] T. Wagner, Particlesizer 1.0.9 (2017).

[52] H. Brenner, The stokes resistance of a slightly deformed sphere, Chem. Eng. Sci. **19,** 519 (1964).

[53] S. Chapman, T. G. Cowling, and D. Burnett, *The Mathematical Theory of Non-Uniform Gases: An Account of the Kinetic Theory of Viscosity, Thermal Conduction and Diffusion in Gases* (Cambridge University Press, Cambridge, United Kingdom, 1990).

[54] G. W. Mulholland, M. K. Donnelly, C. R. Hagwood, S. R. Kukuck, V. A. Hackley, and D. Y. Pui, Measurement of 100 nm and 60 nm particle standards by differential mobility analysis, J. Res. Natl. Inst. Stand. Technol. **111,** 257 (2006).

[55] J. Millen, T. Deesuwan, P. Barker, and J. Anders, Nanoscale temperature measurements using non-equilibrium brownian dynamics of a levitated nanosphere, Nat. Nanotechnol. **9,** 425 (2014).

[56] J. Tellinghuisen, Statistical error propagation, J. Phys. Chem. A **105,** 3917 (2001).

[57] D. W. Allan, Statistics of atomic frequency standards, IEEE **54,** 221 (1966).

[58] F. Czerwinski, A. C. Richardson, and L. B. Oddershede, Quantifying noise in optical tweezers by allan variance, Opt. Express **17,** 13255 (2009).

[59] L. P. Kadanoff, Turbulent heat flow: Structures and scaling, Phys. Today **54,** 34 (2001).

[60] G. Falkovich and K. R. Sreenivasan, Lessons from hydrodynamic turbulance, Phys. Today **59,** 43 (2006).